Dynamic Models for Electrically Excited Synchronous Machines based on Flux-to-Current and Current-to-Inductance Maps

Original
Dynamic Models for Electrically Excited Synchronous Machines based on Flux-to-Current and Current-to-Inductance Maps / Perilli, L., Graffeo, F., Rubino, S., Vaschetto, S.. - ELETTRONICO. - (2024), pp. 5588-5595. (2024 IEEE Energy Conversion Congress and Exposition (ECCE) Phoenix, Arizona, USA 20-24 October 2024) [10.1109/ecce55643.2024.10861168].

Publisher:
Institute of Electrical and Electronics Engineers Inc.

Published
DOI:10.1109/ecce55643.2024.10861168

Dynamic Models for Electrically Excited Synchronous Machines based on Flux-to-Current and Current-to-Inductance Maps

Lorenzo Perilli
Student Member, IEEE
Dipartimento Energia
Politecnico di Torino
Turin, Italy
lorenzo.perilli@polito.it

Federica Graffeo
Member, IEEE
Dipartimento Energia
Politecnico di Torino
Turin, Italy
federica.graffeo@polito.it

Sandro Rubino
Member, IEEE
Dipartimento Energia
Politecnico di Torino
Turin, Italy
sandro.rubino@polito.it

Silvio Vaschetto
Senior Member, IEEE
Dipartimento Energia
Politecnico di Torino
Turin, Italy
silvio.vaschetto@polito.it

***Abstract*—The electrically excited synchronous machine represents a suitable permanent magnet-free alternative for transportation applications. The regulation of the excitation flux, enabled by the presence of the rotor winding, allows high efficiency and power factor operations in a wide speed range. However, the mathematical modeling of these machines becomes non-trivial due to the additional degree of freedom introduced by the rotor current, particularly when considering the magnetic saturation nonlinearities. In such context, this paper presents a dynamic modeling approach for electrically excited synchronous machines for numerical simulations, taking into account the magnetic saturation. An innovative method to obtain the flux-to-current maps is developed for providing the machine model with enhanced simulation capabilities. Dynamic simulations are performed by means of the presented approach and compared to the state-of-the-art models, using the data of a 100 kW sample of the Renault ZOE motor.**

Keywords—electrically excited synchronous motor, wound field synchronous motor, flux-to-current models, dynamic modeling, flux maps.

I. INTRODUCTION

In recent years, electrically excited synchronous machines (EESMs), also known as wound rotor synchronous machines, have become increasingly widespread in the transport sector [1]-[5]. An important reason contributing to their popularity is the absence of permanent magnets (PMs) on the rotor, since the PMs are subject to uncertain availability, large price oscillations and to demagnetization risks [6]. In the EESM, the excitation field is created by means of the rotor current, allowing regulating the excitation flux. This enables a wide constant power speed range and high performance at partial loads [7]-[8]. In addition to that, the EESM topology features fail-safe characteristics, as it can be de-energized by removing the rotor field current, in the case of a fault [9]. However, the losses of the rotating winding result in a limited cooling capability, with respect to the PM machines [10]. Regarding the current supply and the connection to the rotor circuit, brushes and slip rings represent the most commonly adopted choice [4]-[5]. In order to reduce maintenance and improve reliability, contactless configurations featuring capacitive or inductive couplings have been proposed as alternatives to the rotor brushed contacts [11]-[12]. Also, three-stage brushless excitation systems are typically adopted for safety critical aerospace applications, where EESMs have been extensively used as starter/generators in passenger class aircraft [13]-[14].

In this scenario, accurate dynamic modeling of electrically excited synchronous machines is required to perform reliable numerical simulations, for Hardware-in-the-Loop tests and for implementation of control algorithms [15]-[18]. However, the mathematical modeling of EESMs can be a non-trivial task, due to the added complexity introduced by the rotor current, especially when considering the iron saturation [19]-[20]. Different dynamic modeling approaches can be found in the technical literature, many of which are developed for circuit-based simulation software [21]-[23]. In these models, the nonlinearities are approximated through a magnetic saturation curve, which relates the magnetizing machine current to the magnetizing flux linkage [24]-[26]. In order to achieve a more accurate dynamic modeling, the relationships between flux linkages and machine currents can be considered using maps. Indeed, the maps directly relate stator and rotor currents to the fluxes, without introducing approximating functions to model the nonlinearities. Three types of maps are generally adopted for the implementation of dynamic simulations:

- current-to-flux $\boldsymbol{\lambda} = \boldsymbol{\lambda}(\boldsymbol{i})$: the machine currents are used to determine the flux linkages. These maps can be derived by means of finite element analysis or tests;
- current-to-inductance $\boldsymbol{l} = \boldsymbol{l}(\boldsymbol{i})$: the machine currents are used to determine the incremental inductances, computed as the gradients of the fluxes with respect to the currents;
- flux-to-current $\boldsymbol{i} = \boldsymbol{i}(\boldsymbol{\lambda})$: the flux linkages are used to determine the machine currents and can be derived by inversion of the current-to-flux relationships.

These maps are adopted in the implementation of state variable-based simulation models. Depending on the chosen model formulation, one or more of the maps are used. This paper presents state-of-the-art nonlinear dynamic models for EESMs and proposes an innovative procedure to compute the flux-to-current maps for their implementation in numerical environments, such as MATLAB/Simulink. Simulations are performed by means of the presented models, using the data from a 100 kW sample of the EESM equipping the Renault ZOE. The models are compared in terms of results accuracy, computational efficiency and simulation capabilities.

II. EESM DYNAMIC MODELING

The nonlinear dynamic models for the state variable-based simulation environments usually rely on the machine current-to-flux maps $\boldsymbol{\lambda} = \boldsymbol{\lambda}(\boldsymbol{i})$, defined as in (1).

$$\begin{cases} \lambda_d = \lambda_d(i_d, i_q, i_f) \\ \lambda_q = \lambda_q(i_d, i_q, i_f) \\ \lambda_f = \lambda_f(i_d, i_q, i_f) \end{cases} \tag{1}$$

In (1), the machine flux linkages depend on the stator *d*- and *q*- current components and on the field *f*- current. An example of the current-to-flux maps, determined for the 100 kW EESM sample, is provided in Fig. 1. Using to the machine magnetic symmetry, only positive stator *q*-axis currents and positive field currents have been considered in the definition of the represented current-to-flux maps.

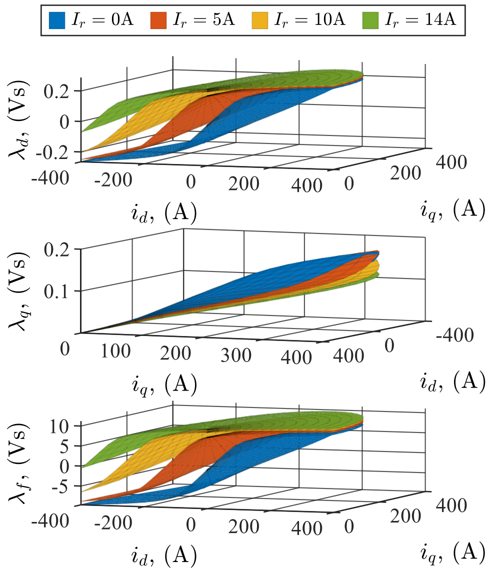

Fig. 1. Current-to-flux maps for the EESM.

The current-to-flux maps can be either used to compute the current-to-inductance or the flux-to-current maps, leading to two alternative modeling approaches, commonly referred to as *'current-based'* and *'flux-based'* models.

A. Current-based model

The current-based model utilizes the currents as state variables and relies on the current-to-flux $\boldsymbol{\lambda}(\boldsymbol{i})$ and current-to-inductance $\boldsymbol{l}(\boldsymbol{i})$ maps. Following the schematic representation in Fig. 2, and neglecting the iron losses and the presence of any rotor damper winding, the current-based dynamic model of the EESM in the *dq* synchronous reference frame is:

$$\frac{d\boldsymbol{i}}{dt} = \boldsymbol{l}^{-1}(\boldsymbol{i})[\boldsymbol{v} - \mathbf{R}\boldsymbol{i} - \omega_e \mathbf{J}\boldsymbol{\lambda}(\boldsymbol{i})] \tag{2}$$

where $\boldsymbol{i} = [i_d \; i_q \; i_f]^{\mathrm{T}}$, $\boldsymbol{\lambda} = [\lambda_d \; \lambda_q \; \lambda_f]^{\mathrm{T}}$ and $\boldsymbol{v} = [v_d \; v_q \; v_f]^{\mathrm{T}}$ are the current, flux linkage and voltage vectors storing the stator and rotor variables, respectively. The machine *d*-axis coincides with the axis of symmetry of the rotor pole and corresponds to the magnetic axis of the rotor winding, whose electrical angular position is defined with respect to the magnetic axis of the first stator phase.

In (2), ω_e is the electrical pulsation, **R** contains the stator $\mathrm{R_s}$ and rotor $\mathrm{R_f}$ resistances and **J** is the rotational matrix for the motional electromotive force calculation:

$$\mathbf{R} = \begin{bmatrix} \mathrm{R_s} & 0 & 0 \\ 0 & \mathrm{R_s} & 0 \\ 0 & 0 & \mathrm{R_f} \end{bmatrix}, \mathbf{J} = \begin{bmatrix} 0 & -1 & 0 \\ 1 & 0 & 0 \\ 0 & 0 & 0 \end{bmatrix} \tag{3}$$

The current-to-inductance matrix $\boldsymbol{l}(\boldsymbol{i})$, which contains the gradients of the flux linkages with respect to the machine currents, is formulated as in (4).

$$\boldsymbol{l}(\boldsymbol{i}) = \begin{bmatrix} l_{dd} = \frac{\partial \lambda_d}{\partial i_d} & l_{dq} = \frac{\partial \lambda_d}{\partial i_q} & l_{df} = \frac{\partial \lambda_d}{\partial i_f} \\ l_{qd} = \frac{\partial \lambda_q}{\partial i_d} & l_{qq} = \frac{\partial \lambda_q}{\partial i_q} & l_{qf} = \frac{\partial \lambda_q}{\partial i_f} \\ l_{fd} = \frac{\partial \lambda_f}{\partial i_d} & l_{fq} = \frac{\partial \lambda_f}{\partial i_q} & l_{ff} = \frac{\partial \lambda_f}{\partial i_f} \end{bmatrix} \tag{4}$$

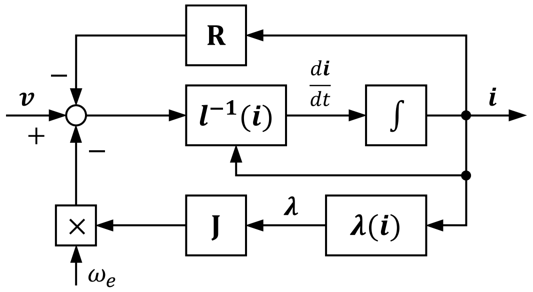

Fig. 2. EESM current-based dynamic model.

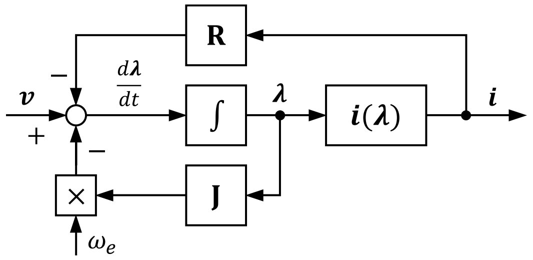

Fig. 3. EESM flux-based dynamic model.

The main benefit of the current-based model is the straightforward determination of the maps needed for its implementation in numerical simulations. However, being the current-to-flux maps nonlinear, each element of the current-to-inductance matrix depends on the *d*-, *q*- and *f*-currents. Therefore, 12 interpolations are performed at every time step, 9 of which are needed for $\boldsymbol{l}(\boldsymbol{i})$ and the remaining for $\boldsymbol{\lambda}(\boldsymbol{i})$. Moreover, as can be noted in Fig. 2, the inversion of the current-to-inductance matrix is required for each step.

In order to the improve the model numerical efficiency, the law of conservation of energy can be applied to exploit linear relations among the matrix elements (e.g., $l_{qd} = l_{dq}$), reducing the number of interpolations to 6, as observed in [27]. In addition, the inverse of $\boldsymbol{l}(\boldsymbol{i})$ can be computed offline, i.e., prior to the dynamic simulation, thus avoiding the online matrix inversion. Nevertheless, the convergence of the current-based model is sensitive to $\boldsymbol{l}(\boldsymbol{i})$ and to its inverse, as they directly establish the current time derivates. Therefore, implementing these assumptions may lead to convergence issues for the model in the case of large data interpolation or extrapolation, strong noise and measurement errors.

B. Flux-based model

The flux-based model utilizes the flux linkages as state variables and relies only on the flux-to-current $\boldsymbol{i}(\boldsymbol{\lambda})$ maps. Under the same assumptions adopted for the current-based, the EESM flux-based model, schematically shown in Fig. 3, is formulated as follows:

$$\frac{d\boldsymbol{\lambda}}{dt} = \boldsymbol{v} - \mathbf{R}\boldsymbol{i} - \omega_e \mathbf{J}\boldsymbol{\lambda} \tag{5}$$

$$\boldsymbol{i} = \boldsymbol{i}(\boldsymbol{\lambda}) \tag{6}$$

The numerical integration of the fluxes time derivatives only requires the interpolation of 3 flux-to-current maps, for retrieving the currents from the fluxes. The reduced number of maps used in the simulation improves the computational efficiency, with respect to the current-based model. However, the flux-to-current maps determination is a more complex and time-consuming task, compared to the computation of $\boldsymbol{l}(\boldsymbol{i})$. Indeed, the determination of $\boldsymbol{i}(\boldsymbol{\lambda})$ consists of interpolating the

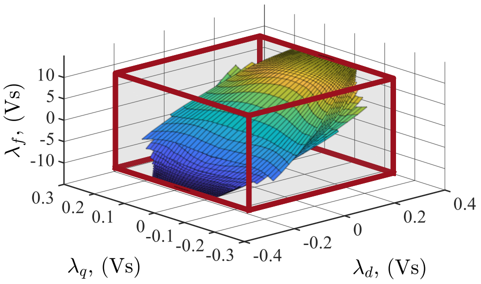

Fig. 4. Fluxes of the current-to-flux maps and smaller external cuboid.

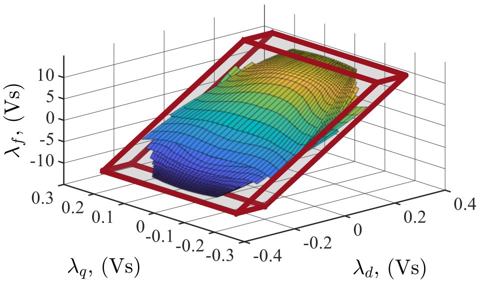

Fig. 5. Fluxes domain in the transformed coordinate system.

current values contained in $\boldsymbol{\lambda}(\boldsymbol{i})$ to obtain a regular mesh grid in the fluxes space, which is non-trivial due to the flux values irregular shape in the considered space, as shown in Fig. 4.

The easiest choice for the definition of a regular flux-to-current domain consists of the smallest cuboid enclosing all the flux values in $\boldsymbol{\lambda}(\boldsymbol{i})$, as shown by the red outline of Fig. 4. However, in this case, the points located in the cuboid empty spaces are computed by extrapolation, since they do not belong to the original maps. The consequent drawback is the poor accuracy of the flux-to-current maps in the extrapolated regions. Moreover, an adequate mesh grid in the area of the original maps requires an excessively fine discretization for the whole cuboid. An alternative is represented by the largest cuboid entirely enclosed by the fluxes of $\boldsymbol{\lambda}(\boldsymbol{i})$, which implies the loss of most of the original data, since a significant number of points is located outside the cuboid. Neither of the two domain choices can provide an accurate and exhaustive formulation of the flux-to-current relationships.

A numerically efficient solution to determine $\boldsymbol{i} = \boldsymbol{i}(\boldsymbol{\lambda})$ is presented in [28], hereafter referred to as '*single step flux-to-current model*', relying on a reference system transformation for the flux vector components.

III. SINGLE STEP FLUX-TO-CURRENT MODEL

As proposed in [28], a prism tightly enclosing the fluxes is defined through a coordinate system transformation. As shown in Fig. 5, the extrapolated points are heavily reduced. For the considered procedure, a 3x3 transformation matrix $\mathbf{G}_\lambda$ is defined to convert the coordinates representation of the flux vector $\boldsymbol{\lambda}$ into a new reference system. For this purpose, the covariance of the fluxes in the current-to-flux maps is computed. The transformation matrix is then retrieved from the eigenvectors and eigenvalues of the fluxes covariance.

According to the considered procedure, the fluxes values for the $\boldsymbol{i}(\boldsymbol{\lambda})$ maps are defined in the new reference system. For each flux vector, an optimization procedure is carried out to identify the current vector whose corresponding flux values differ from the references within a defined tolerance.

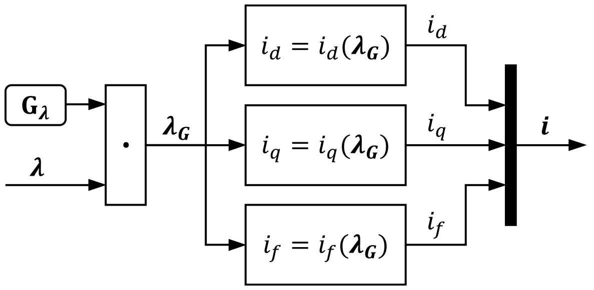

Fig. 6. Single step flux-to-current model solution scheme.

Being $\boldsymbol{\lambda_G} = [\lambda_{dG}\ \lambda_{qG}\ \lambda_{fG}]^{\mathrm{T}}$ the flux vector represented in the new reference system, the optimization procedure leads to the flux-to-current model formulated in (7).

$$\begin{cases} i_d = i_d(\lambda_{dG}, \lambda_{qG}, \lambda_{fG}) \\ i_q = i_q(\lambda_{dG}, \lambda_{qG}, \lambda_{fG}) \\ i_f = i_f(\lambda_{dG}, \lambda_{qG}, \lambda_{fG}) \end{cases} \tag{7}$$

In order to perform numerical simulations, the obtained flux-to-current maps for the new reference system are loaded into the state variable-based environment, together with the corresponding transformation matrix. As shown in the model solution scheme of Fig. 6, at every simulation instant, the flux vector $\boldsymbol{\lambda}$ is modified by means of (8), allowing to compute $\boldsymbol{\lambda_G}$ in the transformed reference system. Since the flux-to-current maps are defined in the new reference system, (7) can be used to retrieve the current vector for the considered time step.

$$\boldsymbol{\lambda_G} = \mathbf{G}_\lambda \cdot \boldsymbol{\lambda} \tag{8}$$

Although the presented model implements a numerically efficient formulation of $\boldsymbol{i}(\boldsymbol{\lambda})$, there are still points computed by extrapolation. In addition, the accuracy of the flux-to-current maps is affected by the tolerance value chosen for the optimization procedure.

IV. TWO-STEP FLUX-TO-CURRENT MODEL

In order to avoid the usage of iterative procedures and data extrapolation, an alternative formulation of the $\boldsymbol{i}(\boldsymbol{\lambda})$ maps is developed in this paper. The proposed approach consists of the following set of equations:

$$i_d = i_d(\lambda_{d,pu}, \lambda_{q,pu}, i_f) \tag{9}$$

$$i_q = i_q(\lambda_{d,pu}, \lambda_{q,pu}, i_f) \tag{10}$$

$$i_f = i_f(i_d, i_q, \lambda_{f,pu}) \tag{11}$$

where $\lambda_{d,pu}$, $\lambda_{q,pu}$ and $\lambda_{f,pu}$ are the per unit values of the flux vector components. The relationships (9) and (10) constitute the stator flux-to-current model, while (11) refers to the rotor. All the maps are computed offline according to the following procedure and used in the simulation environment together with the normalization boundaries for the per unit fluxes.

The stator flux-to-current maps determination consists of interpolating the stator current values for a regular grid in the fluxes domain. For this purpose, the procedure is carried out starting from the relationship (12) derived for a constant rotor current. As can be noted in Fig. 7a, the stator fluxes domain corresponding to (12) is not regular and needs manipulations to obtain a regularly meshed stator flux-to-current model.

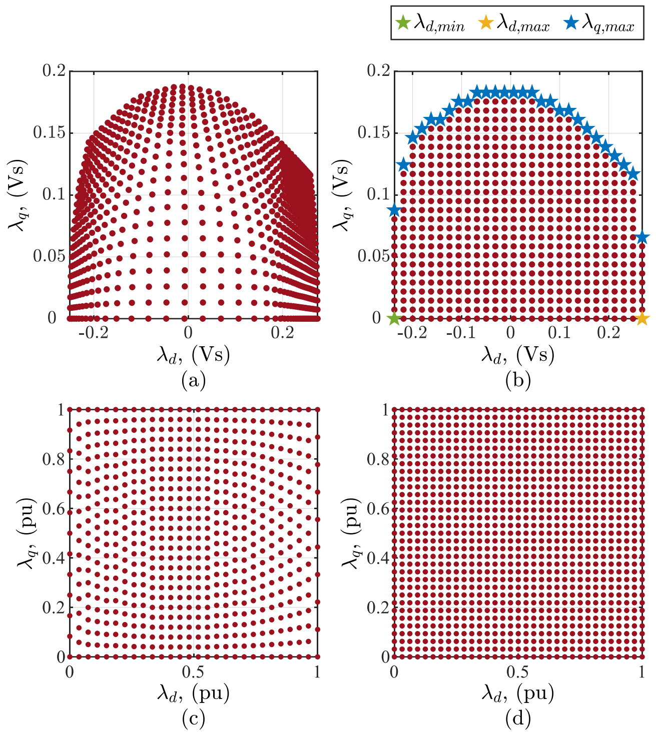

(a) (b) (c) (d)

Fig. 7. Sequence (a)-to-(d) for the stator flux-to-current model determination at a fixed rotor current: (a) starting stator flux components from the current-to-flux maps, (b) stator fluxes in a regularized grid, (c) normalized stator fluxes, (d) normalized stator fluxes in the regularized grid.

$$\begin{cases}\lambda_d = \lambda_d(i_d, i_q)\\ \lambda_q = \lambda_q(i_d, i_q)\end{cases} \tag{12}$$

Therefore, a new regular fluxes domain is created in the space of λ_d and λ_q, as shown in Fig. 7b. In order to define a regular fluxes grid for the stator flux-to-current model valid for all the rotor currents, the fluxes values are normalized within the boundaries $\lambda_{d,min}$, $\lambda_{d,max}$ and $\lambda_{q,max}$. Hence, the per unit values in Fig. 7c are obtained. It should be noted that $\lambda_{d,min}$ and $\lambda_{d,max}$ depend on the i_f level, while $\lambda_{q,max}$ is a function of both i_f and λ_d. The minimum and maximum stator d- and q- fluxes must be stored for later usage in the numerical simulations. Finally, the normalized stator fluxes are used to obtain the stator current components over a regular grid in the fluxes domain, shown in Fig. 7d, which is kept constant for every rotor current. The stator current-to-flux model (9)-(10) is ultimately determined by iterating the proposed procedure for all the available rotor currents.

As for the rotor flux-to-current model (11), the minimum and maximum rotor flux linkage values are determined for every stator current present in the current-to-flux maps. Such values are then used for the rotor flux normalization, and also stored for the normalization in the numerical simulations. The resulting per unit rotor fluxes allow to completely determine (11) over a regular grid, by means of the current-to-flux maps.

Note that the rotor flux-to-current map is defined as in (11) for current-to-flux maps with a rectangular domain of i_d and i_q. In the case of polar maps, i.e., maps characterized by stator current components in a circular domain, (11) can be defined as a function of the stator current amplitude and angle, without any change in the proposed procedure.

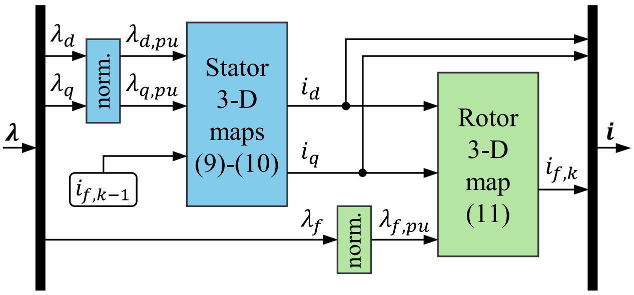

Fig. 8. Two-step flux-to-current model formulation.

Fig. 9. 100 kW EESM sample for the validation current-to-flux data.

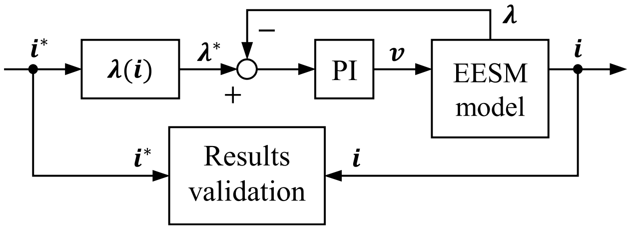

Fig. 10. Control scheme for the fluxes in the closed-loop validation.

Regarding the implementation of the model in numerical simulations, the obtained flux-to-current maps (9)-(11) are loaded in the state variable-based environment, together with the normalization boundaries for the per unit fluxes. As schematically shown in Fig. 8, at every simulation instant, the stator flux components are normalized by means of the boundaries computed in the maps determination procedure. Along with the rotor current of the previous time step $i_{f,k-1}$, $\lambda_{d,pu}$ and $\lambda_{q,pu}$ are used to interpolate the stator 3-D model (9)-(10) and retrieve the d- and q- axes currents. Hence, the stator current components are used with the normalized rotor flux linkage $\lambda_{f,pu}$ to interpolate the rotor 3-D map (11) and compute $i_{f,k}$ for the considered time step.

The proposed EESM flux-based dynamic model features enhanced simulation capabilities, with respect to the single step formulation. Indeed, thanks to the computation of the current vector in two different steps, the benefits are twofold. Firstly, machine dynamic simulations for the stator flux components can be performed for a constant field current. In addition, the proposed flux-to-current model enables accurate simulation of the effects of fast stator current transients on the rotor circuit voltage, by directly acting on i_d and i_q at the output of the stator 3-D maps. For instance, the model second step individually taken allows evaluating the rotor overvoltage caused by a rapid opening of the stator windings, as in the case of inverter fault or overcurrent protection.

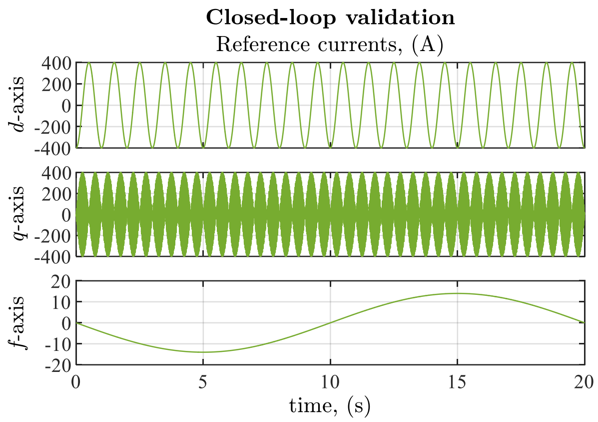

Fig. 11. Reference currents waveforms for the closed-loop simulation.

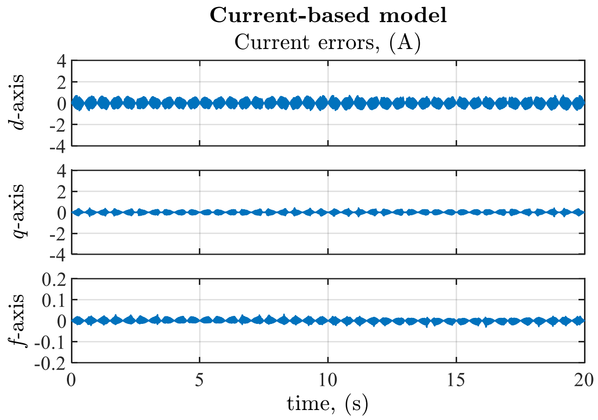

Fig. 12. Errors in i_d, i_q and i_f for the current-based model.

V. NUMERICAL SIMULATIONS

In order to assess the numerical efficiency and the results accuracy of the discussed EESM models (current-based, flux-based single step, flux-based two-step), simulations have been carried out in a state variable-based environment. The data of a 100 kW sample, which is shown in Fig. 9, of the EESM equipping the Renault ZOE have been used for the validation. The windings resistances have been measured by means of DC tests and the values are $R_s = 9.80\ \text{m}\Omega$ and $R_f = 5.67\ \Omega$. The current-to-flux maps for this machine have been derived through finite element analysis considering the maximum stator and rotor currents previously shown in Fig. 1. Lately, the maps have been experimentally verified.

Two approaches have been used for the models numerical validation. In the first one, the models accuracy is analyzed by means of closed-loop control of the fluxes. The references are generated through sinusoidal currents of different frequencies, so as to cover all the domain of the original current-to-flux maps. In the second approach, the models open-loop response to input steps are analyzed. The high dynamics caused by step voltage variations is used to assess the models convergence. In addition, fast stator current transients have been simulated to analyze the consequent rotor overvoltage. For this purpose, only the second step of the proposed flux-based model has been involved in the numerical computation.

A. Results accuracy assessment

The scheme adopted for the machine flux vector control is depicted in Fig. 10. The reference flux vector $\boldsymbol{\lambda}^*$ is generated from a reference current vector $\boldsymbol{i}^*$ by means of the current-to-flux maps. The reference currents used for the validation are three sinusoidal waveforms with different frequencies, as shown in Fig. 11. Depending on the simulation, the block with the EESM model contains one of the three dynamic models considered in this paper. It receives a voltage vector as input and produces current and flux vectors as output. The voltage vector $\boldsymbol{v}$ is generated by the ideal PI regulators, for the *d*-, *q*- and *f*- axes, at a fixed rotational speed of 3000 rpm. Finally, the difference between $\boldsymbol{i}^*$ and the model current $\boldsymbol{i}$ is used to evaluate the results accuracy. The computational efficiency of the models is assessed measuring the simulation time.

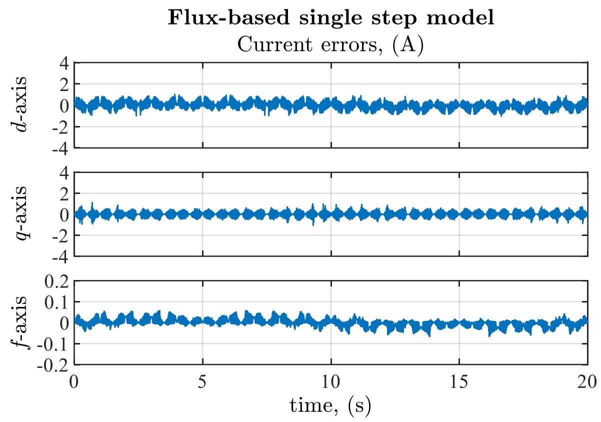

Fig. 13. Errors in i_d, i_q and i_f for the single step flux-based model.

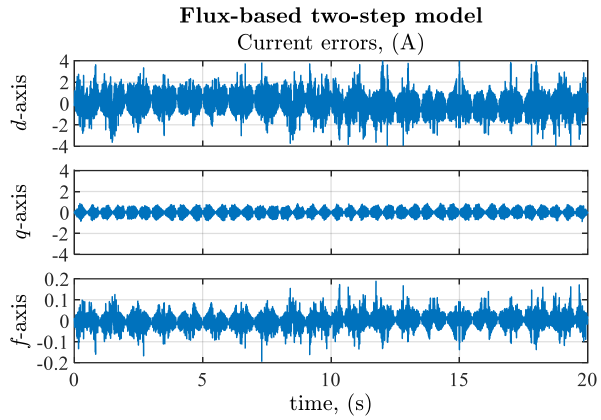

Fig.14. Errors in i_d, i_q and i_f for the two-step flux-based model.

TABLE I. SIMULATIONS RUN TIME FOR THE CLOSED-LOOP RESULTS

Model	run time, (s)
Current-based	55
Flux-based single step	47
Flux-based two-step	38

It should be pointed out that all the 3-D maps considered in the three models are defined only for positive stator *q*-axis currents and positive field currents. The maps are discretized for the same number of points in the three directions (151×151×151). For negative stator *q*-axis and field currents, the maps needed for the current-based and the two-step flux-based models can be derived offline exploiting magnetic symmetries. Conversely, the single step flux-based model relies on an online computation to determine the currents sign, as the magnetic symmetries exploitation is not straightforward in the transformed reference system, thus worsening the numerical efficiency of the single step approach.

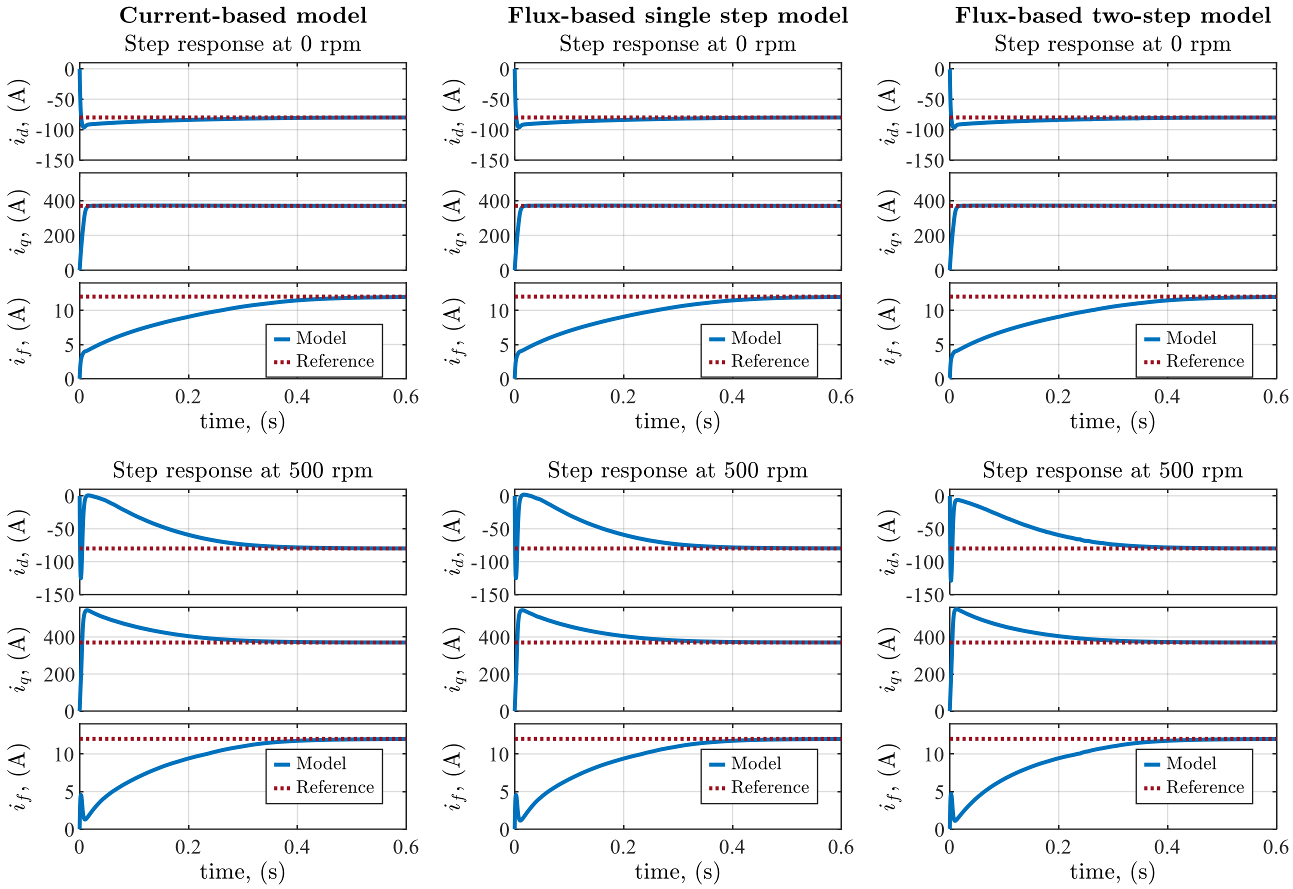

Fig. 15. Responses of the three dynamic models to the step voltages.

The errors between $\boldsymbol{i}^*$ and $\boldsymbol{i}$ for the three dynamic machine models are presented in Figs. 12-14, while Table I collects the run time of the simulations. Except for isolated results outliers, mostly corresponding to unusual machine currents, the accuracy of the proposed two-step flux-based approach is comparable with those of the single step flux-based and current-based models. Note also that the same vertical scales are used for the *d*-, *q*- and *f*- axes errors in Figs. 12-14. Although larger differences are observed for the proposed model, the maximum errors for the three currents are lower than 1.2% of the reference currents at each simulation instant. The relative errors have been computed excluding stator and rotor currents lower than 10 A and 0.35 A, respectively, to avoid the division for relatively small values, thus providing meaningful analyses.

Regarding numerical efficiency, the longest run time is obtained for the current-based model, as a higher number of maps is interpolated at every simulation step, with respect to the two flux-based approaches. The run time discrepancy between the single step and the proposed two-step approaches can be found in the different ways the models deal with negative stator *q*-axis and field currents. The proposed model features the shortest run time, along with high accuracy and additional simulation possibilities in retrieving the rotor flux dynamics, as demonstrated in the following.

B. Models response to input step voltages

The analyses of the responses to input step voltages are necessary to assess the models convergence capabilities in open-loop simulations. Firstly, the step responses with locked rotor are evaluated. Secondly, the rotational speed is set to 500 rpm, to analyze the fluxes variations impact on the convergence. In both cases, the simulation input step voltages are those corresponding to the machine currents in steady-state conditions represented by the dashed lines in Fig. 15. It is possible to observe that, at both speed values, the current transients obtained with the proposed two-step flux-based model are similar to those of the other approaches.

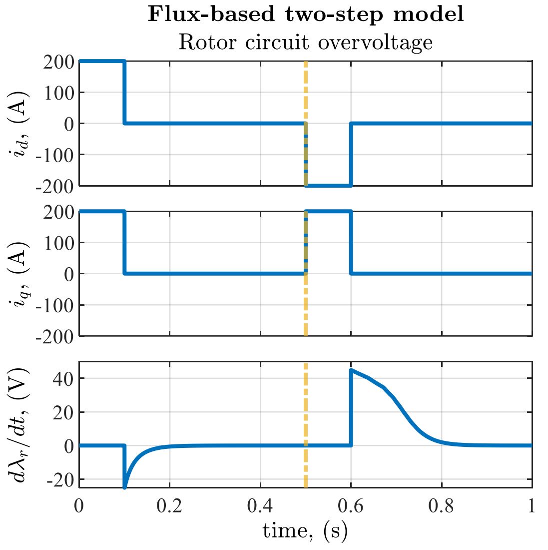

Fig. 16. Rotor overvoltage simulated by means of the two-step model.

C. Rotor overvoltage simulation

The proposed two-step flux-based dynamic model permits to directly provide i_d and i_q to the rotor 3-D map, so as to simulate the rotor flux linkage dynamics. In the numerical validation, the rotor model is supplied with a constant positive input voltage, while the stator currents are imposed as shown in Fig. 16. The simulation output is the rotor flux derivative $d\lambda_r/dt$. The vertical line at 0.5 s corresponds to a reset of the rotor integrator, which is necessary to include only the rotor flux derivatives related to the stator current interruptions in the simulation results. Two different amplitudes are obtained for the flux derivatives, depending on the d-axis current sign prior to the opening.

The smallest overvoltage occurs at the interruption of the positive *d*-axis current, while a larger overvoltage is observed for the interruption of the negative *d*-axis current. Indeed, in the first case, the machine operates in a more saturated condition, as the stator *d*- and rotor currents give concordant contributions to the flux production. Conversely, when the *d*-current opposes the rotor current, the machine operates in a less saturated condition. Therefore, a sudden reduction of the negative *d*-axis current causes a larger change in the rotor flux linkage, resulting in a greater overvoltage.

VI. CONCLUSION

A nonlinear dynamic model based on flux-to-current maps for electrically excited synchronous machines has been developed. The proposed two-step approach for the numerical implementation of the flux-to-current maps provides the model with enhanced simulation capabilities with respect to other modeling approaches found in the technical literature. For comparison purposes, an overview of the state-of-the-art dynamic models for EESMs has been presented, emphasizing the advantages and the challenges of their implementations in state variable-based simulation environments.

The numerical validation of the proposed model has been performed using the data from the 100 kW EESM equipping the Renault ZOE. As presented in the paper, the proposed two-step flux-based model features good computational efficiency, compared to the other approaches in the technical literature, still ensuring significantly low errors for all the machine admissible currents. In addition, the convergence capabilities of the proposed model have been verified by means of high-dynamics simulations exploiting input step voltages. The enhanced possibilities offered by the two-step approach have been also demonstrated in the numerical environment. The rotor flux linkage dynamics has been simulated for two different stator current transients, showing the impact of the magnetic saturation on the rotor overvoltage.

ACKNOWLEDGMENT

This study was carried out within the MOST – Sustainable Mobility National Research Center and received funding from the European Union Next-GenerationEU (PIANO NAZIONALE DI RIPRESA E RESILIENZA (PNRR) – MISSIONE 4 COMPONENTE 2, INVESTIMENTO 1.4 – D.D. 1033 17/06/2022, CN00000023). This manuscript reflects only the authors' views and opinions, neither the European Union nor the European Commission can be considered responsible for them.

REFERENCES

[1] F. Graffeo, S. Vaschetto, A. Tenconi and A. Cavagnino, "Fast Sizing Procedure for Salient-Pole Wound Field Synchronous Motors for Transportation Electrification," 2023 IEEE International Electric Machines & Drives Conference (IEMDC), San Francisco, CA, USA, 2023, pp. 1-7.

[2] F. Graffeo, S. Vaschetto, A. Tenconi and A. Cavagnino, "No-Load Characteristic Computation for Wound Field Synchronous Propulsion Motors," 2023 IEEE International Conference on Electrical Systems for Aircraft, Railway, Ship Propulsion and Road Vehicles & International Transportation Electrification Conference (ESARS-ITEC), Venice, Italy, 2023, pp. 1-6.

[3] F. Graffeo, S. Vaschetto, M. Cossale, M. Kerschbaumer, E. C. Bortoni and A. Cavagnino, "Cylindrical Wound-Rotor Synchronous Machines for Traction Applications," 2020 International Conference on Electrical Machines (ICEM), Gothenburg, Sweden, 2020, pp. 1736-1742.

[4] "RENAULT ZOE E-TECH 100% electric 4th January 2024," [Online]. Available: https://cdn.group.renault.com/ren/gb/transversal-assets/brochures/mobile-brochure-tech-spec/mobile-tech-spec-zoe.pdf (accessed: Jul. 18, 2024).

[5] "Specifications. (from 9/2021 on) BMW iX3.," [Online]. Available: https://www.press.bmwgroup.com/global/article/attachment/T0338848EN/524017 (accessed: Jul. 18, 2024).

[6] Estenlund, M. Alaküla and A. Reinap, "PM-less machine topologies for EV traction: A literature review," 2016 International Conference on Electrical Systems for Aircraft, Railway, Ship Propulsion and Road Vehicles & International Transportation Electrification Conference (ESARS-ITEC), Toulouse, France, 2016, pp. 1-6.

[7] J. de Santiago et al., "Electrical Motor Drivelines in Commercial All-Electric Vehicles: A Review," in *IEEE Transactions on Vehicular Technology*, vol. 61, no. 2, pp. 475-484, Feb. 2012.

[8] C. Rossi, D. Casadei, A. Pilati and M. Marano, "Wound Rotor Salient Pole Synchronous Machine Drive for Electric Traction," Conference Record of the 2006 IEEE Industry Applications Conference Forty-First IAS Annual Meeting, Tampa, FL, USA, 2006, pp. 1235-1241.

[9] V. Madonna, P. Giangrande and M. Galea, "Electrical Power Generation in Aircraft: Review, Challenges, and Opportunities," in *IEEE Transactions on Transportation Electrification*, vol. 4, no. 3, pp. 646-659, Sept. 2018.

[10] I. Boldea, L. N. Tutelea, L. Parsa and D. Dorrell, "Automotive Electric Propulsion Systems With Reduced or No Permanent Magnets: An Overview," in *IEEE Transactions on Industrial Electronics*, vol. 61, no. 10, pp. 5696-5711, Oct. 2014.

[11] D. C. Ludois, J. K. Reed and K. Hanson, "Capacitive Power Transfer for Rotor Field Current in Synchronous Machines," in *IEEE Transactions on Power Electronics*, vol. 27, no. 11, pp. 4638-4645, Nov. 2012.

[12] T. Raminosoa and R. Wiles, "Contactless Rotor Excitation for Traction Motors," 2018 IEEE Energy Conversion Congress and Exposition (ECCE), Portland, OR, USA, 2018, pp. 6448-6453.

[13] E. Sayed et al., "Review of Electric Machines in More-/Hybrid-/Turbo-Electric Aircraft," in *IEEE Transactions on Transportation Electrification*, vol. 7, no. 4, pp. 2976-3005, Dec. 2021.

[14] Y. Wang, S. Nuzzo, H. Zhang, W. Zhao, C. Gerada and M. Galea, "Challenges and Opportunities for Wound Field Synchronous Generators in Future More Electric Aircraft," in *IEEE Transactions on Transportation Electrification*, vol. 6, no. 4, pp. 1466-1477, Dec. 2020.

[15] S. Rubino, I. R. Bojoi, E. Armando and A. Tenconi, "Deadbeat Direct Flux Vector Control of Surface Permanent Magnet Motor Drives," in *IEEE Transactions on Industry Applications*, vol. 56, no. 3, pp. 2685-2699, May-June 2020.

[16] A. Amerise, M. Mengoni, L. Zarri, A. Tani, S. Rubino and R. Bojoi, "Open-End Windings Induction Motor Drive With Floating Capacitor Bridge at Variable DC-Link Voltage," in *IEEE Transactions on Industry Applications*, vol. 55, no. 3, pp. 2741-2749, May-June 2019.

[17] J. S. Lee and G. Choi, "Modeling and hardware-in-the-loop system realization of electric machine drives — A review," in *CES Transactions on Electrical Machines and Systems*, vol. 5, no. 3, pp. 194-201, Sept. 2021.

[18] S. Rubino, R. Bojoi, E. Levi and O. Dordevic, "Vector Control of Multiple Three-Phase Permanent Magnet Motor Drives," IECON 2018 - 44th Annual Conference of the IEEE Industrial Electronics Society, Washington, DC, USA, 2018, pp. 5866-5871.

[19] E. Levi, "Saturation modelling in d-q axis models of salient pole synchronous machines," in *IEEE Transactions on Energy Conversion*, vol. 14, no. 1, pp. 44-50, March 1999.

[20] E. Levi and V. A. Levi, "Impact of dynamic cross-saturation on accuracy of saturated synchronous machine models," in *IEEE Transactions on Energy Conversion*, vol. 15, no. 2, pp. 224-230, June 2000.

[21] D. C. Aliprantis, S. D. Sudhoff and B. T. Kuhn, "A synchronous machine model with saturation and arbitrary rotor network representation," in *IEEE Transactions on Energy Conversion*, vol. 20, no. 3, pp. 584-594, Sept. 2005.

[22] D. C. Aliprantis, O. Wasynczuk and C. D. RodrÍguez Valdez, "A Voltage-Behind-Reactance Synchronous Machine Model With Saturation and Arbitrary Rotor Network Representation," in *IEEE Transactions on Energy Conversion*, vol. 23, no. 2, pp. 499-508, June 2008.

[23] A. M. Cramer, B. P. Loop and D. C. Aliprantis, "Synchronous Machine Model With Voltage-Behind-Reactance Formulation of Stator and Field Windings," in *IEEE Transactions on Energy Conversion*, vol. 27, no. 2, pp. 391-402, June 2012.

[24] S.-A. Tahan and I. Kamwa, "A two-factor saturation model for synchronous machines with multiple rotor circuits," in *IEEE Transactions on Energy Conversion*, vol. 10, no. 4, pp. 609-616, Dec. 1995.

[25] K. A. Corzine, B. T. Kuhn, S. D. Sudhoff and H. J. Hegner, "An improved method for incorporating magnetic saturation in the q-d synchronous machine model," in *IEEE Transactions on Energy Conversion*, vol. 13, no. 3, pp. 270-275, Sept. 1998.

[26] S. D. Pekarek, E. A. Walters and B. T. Kuhn, "An efficient and accurate method of representing magnetic saturation in physical-variable models of synchronous machines," in *IEEE Transactions on Energy Conversion*, vol. 14, no. 1, pp. 72-79, March 1999.

[27] P. G. Carlet, L. Cinti, L. Ortombina and N. Bianchi, "Dynamic model for HEPM motors including the nonlinear magnetic characteristics," 2023 IEEE International Electric Machines & Drives Conference (IEMDC), San Francisco, CA, USA, 2023, pp. 1-7.

[28] L. Geier, J. Stoß, A. Liske and M. Hiller, "Generalized Inversion of n-dimensional Flux Maps for Unified Nonlinear Machine Models and Predictive Control Algorithms," 2023 IEEE Energy Conversion Congress and Exposition (ECCE), Nashville, TN, USA, 2023, pp. 4821-4828.